NONLINEAR FREQUENCY RESPONSE ANALYSIS AND JUMP AVOIDANCE DESIGN OF MOLECULAR SPRING ISOLATOR

M.-C. Yu X. Gao Q. Chen*

State Key Laboratory of Mechanics and Control of Mechanical Structures
Nanjing University of Aeronautics and Astronautics
Nanjing, China

ABSTRACT

Molecular spring vibration isolation technology has been invented in the recent years but it still needs further development in dynamics theory. A molecular spring isolation (MSI) consists of water and hydrophobic zeolites as working medium, providing high-static-low-dynamic stiffness. The dynamic properties of MSI are thoroughly investigated in this paper. Firstly, the nonlinear dynamic model of a vibration system support by MSI, i.e. the equation of motion, is established. Then the averaging method is employed to estimate the frequency response function (FRF) of the primary resonance. The phase trajectories diagram evolvement of primary resonance is also investigated to analysis the stability of the primary resonance response. From the plot of FRF, it is found that there exists a jump phenomenon induced by nonlinear stiffness, which may have harmful impacts on the equipment which is supposed to be protected from vibrations and shocks. To avoid jump, the FRF is analyzed to find the critical values of system parameters and a jump avoidance criterion is introduced.

Keywords: Vibration isolation, Molecular spring isolator, High-static-low-dynamic stiffness, Jump phenomenon.

1. INTRODUCTION

The use of passive isolators is one of the most common methods of controlling undesirable vibrations. There are continuing efforts to develop new approaches in order to achieve higher performance [1, 2]. As a novel passive vibration control technology, molecular spring isolator (MSI) starts receiving attention due to its high-static-low-dynamic (HSLD) stiffness properties, which suits for heavy equipment with low frequency [3, 4].

A MSI has a compressible chamber filled with molecular spring material as working medium (see Fig. 1). The molecular spring material is a mixture of water and hydrophobic zeolites. Different with traditional use of nanoporous materials such as silica gel and zeolites, recent study found that water molecules can squeeze into the pores of hydrophobic nano-porous materials under very high hydraulic pressure [5]. During this process, mechanical energy converts into interfacial energy. When the hydraulic pressure drops, there is different phenomenon for different kinds of nano-porous materials. For water and hydrophobic silica gels, the confined liquid would remain in the nano-environment, resulting in a significant hysteresis of sorption isotherm [6-9]. On the contrary, for water and some kinds of hydrophobic zeolites, water molecules extrude from the nano-pores as soon as the pressure drops, resulting in coincidence sorption isotherm [10-14]. For the former, the mechanical energy is absorbed so the mixture of water and hydrophobic silica gels is used as colloidal damper. For water and hydrophobic zeolites, there is a reciprocal trans-

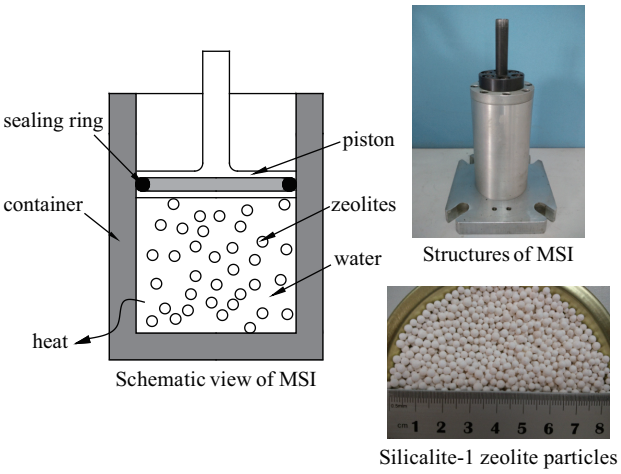


Fig. 1 Structures and material of MSI.

* Corresponding author (Q.Chen@nuaa.edu.cn)

DOI : 10.1017/jmech.2016.52
Copyright © 2016 The Society of Theoretical and Applied Mechanics
https://doi.org/10.1017/jmech.2016.52 Published online by Cambridge University Press

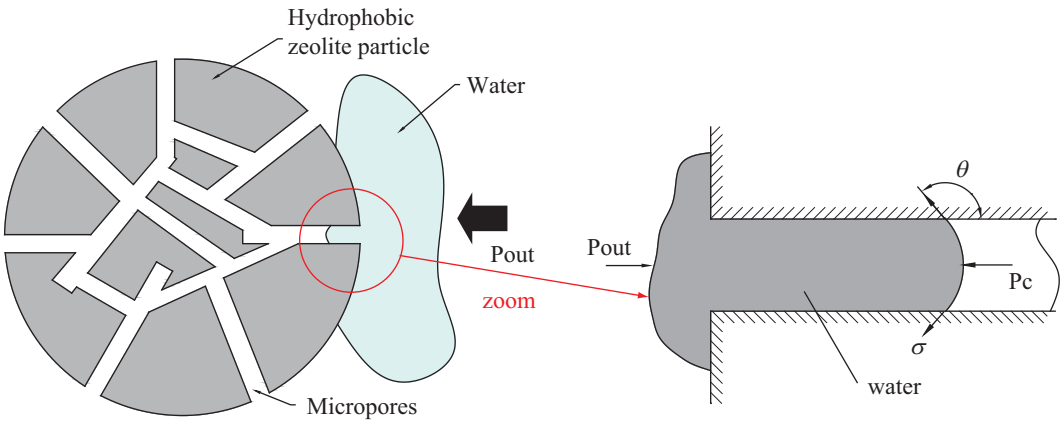


Fig. 2 Laplace capillary pressure.

formation of mechanical energy and interfacial energy, which works like a spring, so it is termed as molecular spring.

The energetic application potential of water and hydrophobic nano-porous materials was first found by Eroshenko [5]. Suciu [6, 7] and Qiao [8-9] tried to use colloidal damper for energy absorption. Eroshenko and Patarin [10-14] start to investigate molecular spring material at the beginning of this century. They have affirmed that several kinds of zeolites such as Silicalite-1, SSZ-24, ZSM-22, ZSM-12, DD3R and Si-CHA can be used as the nano-porous material for molecular spring. Desbiens [15] has undertaken GCMC (Grand Canonical Monte Carlo) simulations of liquid water intrusion into hydrophobic nano-pores of zeolites. However, these researchers mainly work on synthesizing new materials, characterizing zeolites and microscopic working mechanism investigation of molecular spring. The authors of this paper firstly established the mechanical model of MS I and tried to use molecular spring for vibration isolation purpose [3, 4].

In this paper, the dynamic properties of MSI are investigated. A MSI of piston cylinder structure is designed (see Fig. 1). The nonlinear dynamic model of a vibration system support by MSI, i.e. the equation of motion, is established. The Frequency response function (FRF) of the system was analyzed by averaging method. By plotting the FRF, it is found that there exists a jump phenomenon. The jump phenomenon is harmful because it can bring up an unacceptable impact to structures or protected equipment [16], such as marine engines and other rotating machines. To avoid the downside of jump phenomenon, the FRF are analyzed to give jump avoidance criteria.

2. THE MODEL OF MSI ISOLATION SYSTEM

The working principle of molecular spring is that water molecules intrude into and extrude from hydrophobic micropores (pores whose diameter is less than 2 nm as defined by IUPAC [17]) of zeolites (see Fig. 2).

As shown in Fig. 2, for water molecules and a single micropore, water starts to squeeze into the hydrophobic pore when the external pressure P_{out} overcomes the capillary pressure P_c, which belongs to Lapalace-Washbun relation [10, 11]

$$P_c = -2\sigma\cos\theta / r \tag{1}$$

where σ is the surface tension of water, θ is the contact angle of water and solid interface and r is the radius of the pore.

In practical, water molecules intrude into large numbers of pores when MSI is compressed. It is a complex process because the diameter and the hydrophobicity of pores are discrepant from each other. The process of compressing molecular spring can be described as three stages (see Fig. 3).

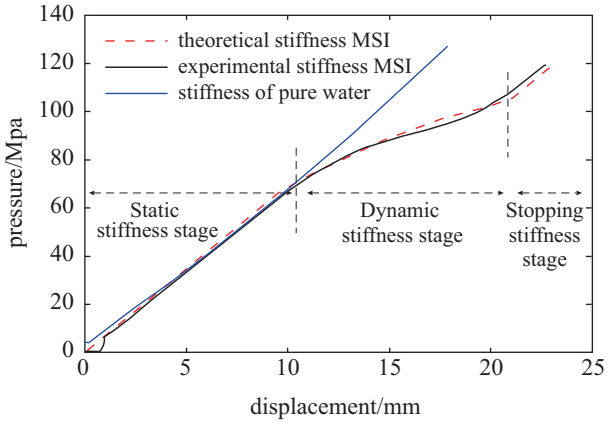


Fig. 3 Experimental stiffness curves of pure water and MSI.

The first stage is the static stiffness stage where the external pressure is insufficient to overcome the capillary pressure and no water molecule intrudes into pores. In this case, it is necessary to consider water as compressible liquid and the compressibility of water contributes all the volume decrement of molecular spring. The compressibility of water is very small so the volume change is very limited. As a result, molecular spring obtains very high static stiffness at this stage.

https://doi.org/10.1017/jmech.2016.52 Published online by Cambridge University Press

The second stage corresponds to the dynamic stiffness stage where hydraulic pressure is high enough. In this stage, water molecules overcome capillary pressure P_c and intrude into pores at a massive scale. The intrusion of water molecules leads to big volume change. As the diameters and contact angles of the pores are different, water molecules firstly fill pores which have biggest apertures and smallest contact angles, and then fill smaller pores with larger contact angles and so on, until all pores are saturated. As a result, MSI exhibits very low stiffness in this stage.

The third compressing stage is stopping stiffness stage where all pores have been filled with water. The compressibility of water determines the stiffness of this stage. Therefore, the molecular spring obtains very high stiffness again which can prevent the vibration system from overshooting.

The stiffness properties of MSI were deserved by integrating the pores volume in our former work [4]. To validate the theory, a quasi-static compress experiment of MSI was also conducted utilizing a static-dynamic universal testing machine. Fig. 3 compares the theoretical and experimental stiffness curves of MSI with compressing pure water. It can be seen that MSI provides nonlinear piecewise stiffness properties.

Figure 4 gives a single degree of freedom vibration system supported by a MSI. With payload of mass, the MSI is compressed to the dynamic stiffness stage. The static equilibrium point changes form Fig. 3 to Fig. 5, i.e. form static stiffness stage to dynamic stiffness stage. Consequently, the MSI isolation system exhibits HSLD stiffness properties as shown in Fig. 5. Take the static equilibrium position as the origin of the coordinate system, therefore, the equation of motion of a MSI vibration system subject to cosine excitation is

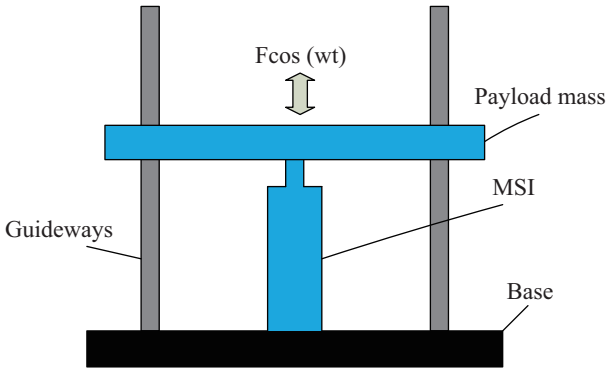


Fig. 4 A single degree of freedom system supported by a MSI.

$$M\ddot{x} + c\dot{x} + f_k(x) = F\cos(\omega t) \tag{2}$$

in which $f_k(x)$ is the restoring force and it has been studied in reference [3], c is the damping coefficient. The damping comes from the structure damping, especially from the friction between piston and sealing ring.

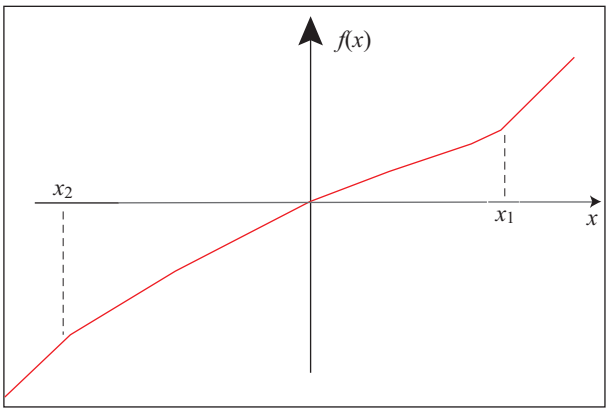


Fig. 5 Stiffness curve of the system supported by a MSI, x_1 and x_2 are critical values of displacement, $x_1 < -x_2$.

$$f_k(x) = \begin{cases} \left(\alpha_1 + \alpha_2 x_1 + \alpha_3 {x_1}^2\right)\cdot x_1 + k_0(x - x_1) & (x > x_1) \\ \alpha_1 x + \alpha_2 x^2 + \alpha_3 x^3 & (x_1 < x < -x_2) \\ \left(\alpha_1 + \alpha_2 x_2 + \alpha_3 {x_2}^2\right)\cdot x_2 + k_0(x - x_2) & (x < -x_2) \end{cases} \tag{3}$$

In Eq. (3), x_1 and x_2 are critical values of displacement, α_1, α_2 and α_3 are nonlinear dynamic stiffness coefficients and k_0 is the static stiffness and stopping stiffness. Eq. (3) gives the piecewise nonlinear restoring force of MSI isolation system.

Figure 6 compares the numerical force transmissibility of MSI isolation system described in Eq. 2 with a conventional linear system. Consider the nonlinearity, the force transmissibility is described as the ratio of root mean square of restoring force and excitation force according to reference [1]. From Fig. 6 we can see that MSI isolation system has better vibration isolation performance than a linear system.

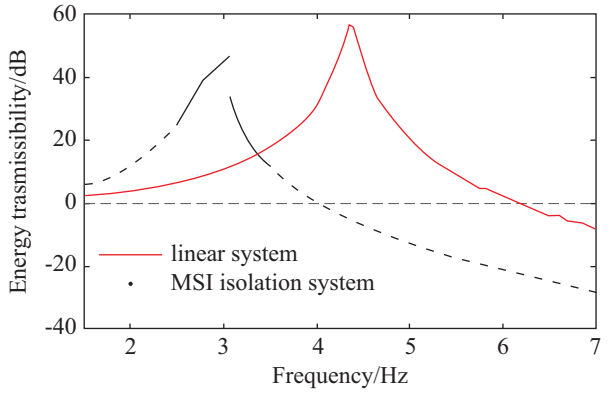


Fig. 6 Numerical force transmissibility of MSI isolation system and a linear system. (MSI isolation system parameters: M =730 Kg, c = 730 Nsm^{-1}, α_1 = 2.3411 × 10^5 Nm^{-1}, α_2 = -8.5706 × 10^{-6} Nm^{-1}, α_3 = 8.7465 × 10^8 Nm^{-1}, k_0 = 5.494 × 10^5, x_1 = 5.3×10^{-3} m, x_2 = -6.7 × 10^{-3} m, F = 130 N. The linear system have the same payload mass and damping coefficient with MSI isolation system and the linear stiffness is k_0 = 5.494 × 10^5).

https://doi.org/10.1017/jmech.2016.52 Published online by Cambridge University Press

3. NONLINEAR FRF ANALYSIS

3.1 FRF of Primary Resonance

Averaging method is employed in this section to develop an expression for the frequency response. Gao *et al*. [16] have validated that averaging method can be used to evaluate the FRF of a piecewise system. To apply averaging method, Eq. (2) is rewritten as

$$\ddot{x}+\omega^2 x=\varepsilon\left(-c_0\dot{x}+f_0\cos(\omega t)-g(x)\right) \tag{4}$$

$$g(x)=\begin{cases}\left(\omega_0^2-\sigma\right)x+fc_1, & (x>x_1)\\ -\sigma x+r_2x^2+r_3x^3, & (x_1<x<-x_2)\\ \left(\omega_0^2-\sigma\right)x+fc_2, & (x<-x_2)\end{cases} \tag{5}$$

In Eq. (4) $\varepsilon=\frac{k_0}{\alpha_1}-1$, $c_0=\frac{c_m}{\varepsilon}$, $c_m=\frac{c}{M}$, $f_0=\frac{f_m}{\varepsilon}$, $f_m=\frac{F}{M}$. As shown in Eq. (5), $g(x)$ is derived from $f_k(x)$ and $\omega_0=\sqrt{\frac{\alpha_1}{m}}$, $\sigma=\frac{1}{\varepsilon}\left(\omega^2-\omega_0^2\right)$, $r_2=\frac{\alpha_2}{M\varepsilon}$, $r_3=\frac{\alpha_3}{M\varepsilon}$, $fc_1=\frac{\alpha_1x_1+\alpha_2x_1^2+\alpha_3x_1^3-k_0x_1}{M\varepsilon}$, $fc_2=\frac{\alpha_1x_2+\alpha_2x_2^2+\alpha_3x_2^3-k_0x_2}{M\varepsilon}$.

After the transient response has died out, we consider a solution in the form of $x=a(t)\cos(\omega t-\theta)$ as a first-order trial solution (see Fig. 7). In the first-order trial solution, a is the displacement amplitude and θ is the phase. Assuming $\varphi=\omega t-\theta$ and applying averaging method to Eq. (4)

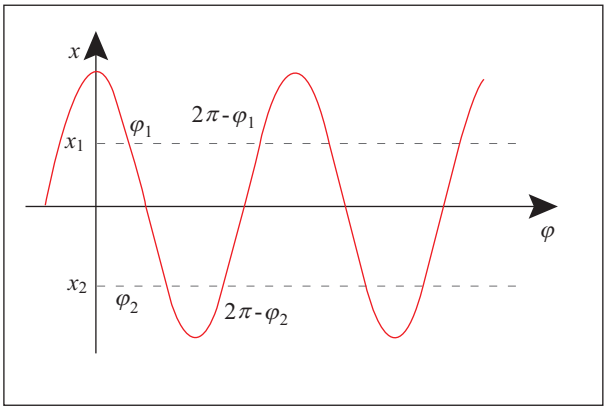


Fig. 7 Steady state response, φ_1 and φ_2 are critical phase angles at critical displacement.

$$\dot{a}=-\frac{\varepsilon}{\omega}\cdot\frac{1}{2\pi}\int_0^{2\pi}f\left(a\cos(\varphi),-a\omega\sin(\varphi)\right)\sin(\varphi)\,d\varphi=-\frac{\varepsilon}{2\omega}\left(\Phi(a,\omega)-f_0\sin(\theta)\right) \tag{6}$$

$$\dot{\theta}=\frac{\varepsilon}{\omega a}\cdot\frac{1}{2\pi}\int_0^{2\pi}f\left(a\cos(\varphi),-a\omega\sin(\varphi)\right)\cos(\varphi)\,d\varphi=\frac{\varepsilon}{2\omega a}\left(\Psi(a,\omega)+f_0\cos(\theta)\right) \tag{7}$$

in which

$$\Phi(a,\omega)=\frac{1}{\pi}\int_0^{2\pi}-\left(-c_0a\omega\sin(\varphi)+g\left(a\cos(\varphi)\right)\right)\sin(\varphi)\,d\varphi \tag{8}$$

$$\Psi(a,\omega)=\frac{1}{\pi}\int_0^{2\pi}-\left(-c_0a\omega\sin(\varphi)+g\left(a\cos(\varphi)\right)\right)\cos(\varphi)\,d\varphi \tag{9}$$

The FRF is expressed by an implicit function

$$\Phi^2+\Psi^2+f_0^2=0 \tag{10}$$

And the phase characteristics is

$$\tan(\theta)=-\frac{\Phi}{\Psi} \tag{11}$$

For a piecewise system, Φ and Ψ are calculated piecewise because the integral interval changes when the amplitude a crosses the critical values of displacement. Without loss of generality, we assume that $x_1 < -x_2$.

i. If a< x_1, only dynamic stiffness stage is included in $g(x)$ so it can be simplified as follows

$$g_1\left(a\cos(\varphi)\right)=-\sigma\cdot a\cos(\varphi)+r_2\left(a\cos(\varphi)\right)^2+r_3\left(a\cos(\varphi)\right)^3,\ (0\le\varphi\le2\pi) \tag{12}$$

We define that $\lambda=\omega/\omega_0$. From integral we can get

https://doi.org/10.1017/jmech.2016.52 Published online by Cambridge University Press

$$\Phi_1 = c_0 a\lambda\omega_0 \tag{13}$$

$$\Psi_1 = -\frac{1}{4}a\left(-4\sigma + 3r_3a^2\right) \tag{14}$$

ii. If x_1<a< $-x_2$, dynamic stiffness and stopping stiffness are included in $g(x)$ so it can be rewritten as follows

$$g_2\left(a\cos(\varphi)\right) = \begin{cases} \left(\omega_0^2 - \sigma\right)\cdot a\cos(\varphi) + fc_1, & (0 \le \varphi < \varphi_1, 2\pi - \varphi_1 \le \varphi \le 2\pi) \\ -\sigma\cdot a\cos(\varphi) + r_2\left(a\cos(\varphi)\right)^2 + r_3\left(a\cos(\varphi)\right)^3, & (\varphi_1 \le \varphi < 2\pi - \varphi_1) \end{cases} \tag{15}$$

From piecewise integral we can get

$$\Phi_2 = c_0 a\lambda\omega_0 \tag{16}$$

$$\begin{aligned}\Psi_2 = -\frac{1}{12\pi}(&12\omega_0 x_1 R_1 + 12a\omega_0^2\gamma_1 + 24fc_1R_1 - 8r_2x^2R_1 - 9r_3a^2\gamma_1 - 16a^2r_2R_1 - 6r_3x_1^3R_1 \\ &- 9r_3a^3x_1R_1 - 12a\sigma\pi + 9r_3a^3\pi)\end{aligned} \tag{17}$$

in which $R_1 = \sqrt{(a^2 - x_1^2)/a^2}$, $\gamma_1 = \arccos(x_1/a)$.

iii. If $a >$- x_2, dynamic stiffness, stopping stiffness and static stiffness are all included in $g(x)$ so

$$g_3\left(a\cos(\varphi)\right) = \begin{cases} \left(\omega_0^2 - \sigma\right)\cdot a\cos(\varphi) + fc_1, & (0 \le \varphi < \varphi_1, 2\pi - \varphi_1 \le \varphi \le 2\pi) \\ -\sigma\cdot a\cos(\varphi) + r_2\left(a\cos(\varphi)\right)^2 + r_3\left(a\cos(\varphi)\right)^3, & (\varphi_1 \le \varphi < \varphi_2, 2\pi - \varphi_2 \le \varphi < 2\pi - \varphi_1) \\ \left(\omega_0^2 - \sigma\right)\cdot a\cos(\varphi) + fc_2, & (\varphi_2 \le \varphi < 2\pi - \varphi_2) \end{cases} \tag{18}$$

From piecewise integral we can get

$$\Phi_3 = c_0 a\lambda\omega_0 \tag{19}$$

$$\begin{aligned}\Psi_3 = -\frac{1}{12\pi}(&-12a\sigma\pi + 12a\omega_0^2\pi + 12\omega_0^2 x_1R_1 + 24fc_1R_1 - 12a\omega_0^2\gamma_2 - 24fc_2R_2 - 12\omega_0^2x_2R_2 + 12a\omega_0^2\gamma_1 9r_3a^2x_1R_1 \\ &- 8r_2x_1^2R_1 - 16a^2r_2R_1 - 6r_3x_1^3R_1 - 9r_3a^3\gamma_1 + 8r_2x_2^2R_2 + 16a^2r_2R_2 + 6r_3x_2^3R_2 + 9r_3a^2x_2R_2 + 9r_3a^3\gamma_2)\end{aligned} \tag{20}$$

in which $R_2 = \sqrt{(a^2 - x_2^2)/a^2}$, $\gamma_2 = \arccos(x_2/a)$.

We define the maximum value of a over the whole frequency range as A. There are three situations of FRF considering A changes with the excitation force.

If $A < x_1$, the FRF of whole frequency range can be plotted by substituting Eq. (13) and (14) into Eq. (10). So Eq. (10) is rewritten as

$$\Phi_1^2 + \Psi_1^2 + f_0^2 = 0, \qquad (a < x_1) \tag{21}$$

The theoretical expression of FRF is considered as the analytic FRF, which is actually the theoretical approximation of real FRF. The numerical FRF is also calculated by fourth order Runge-Kutta method and it is considered as the exact solution. The analytic FRF from Eq. 21 is compared with numerical FRF in Fig. 8.

If $x_1 < A <$ $-x_2$, the FRF consists of two parts becasue displacement amplitude changes across critical displacement when excitation frequency varies. Eq. (10) is rewritten as follows

$$\begin{cases} \Phi_1^2 + \Psi_1^2 + f_0^2 = 0, & (a < x_1) \\ \Phi_2^2 + \Psi_2^2 + f_0^2 = 0, & (x_1 < a < -x_2) \end{cases} \tag{22}$$

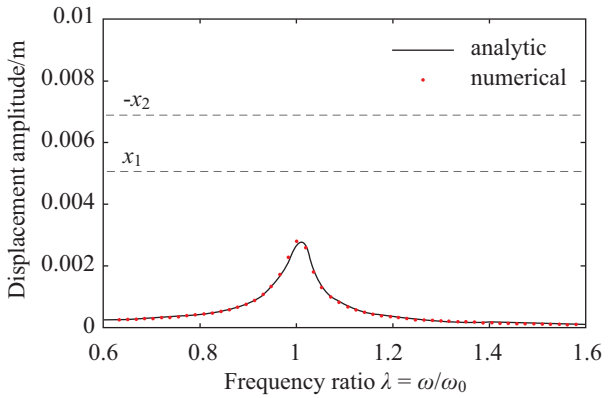


Fig. 8 Analytic FRF and numerical FRF of MSI system with initial condition (0, 0), $F/M = 0.05$.

The two parts in Eq. (22) join together at the critical displacement x_1. Fig. 9 compares the analytic FRF and numerical FRF of $x_1 < A <$ $-x_2$.

If $A >$ - x_2, the FRF consists of three parts including $a < x_1$ part, $x_1 < a <$ $-x_2$ part and a > $-x_2$ part. Eq. (10) is rewritten as

https://doi.org/10.1017/jmech.2016.52 Published online by Cambridge University Press

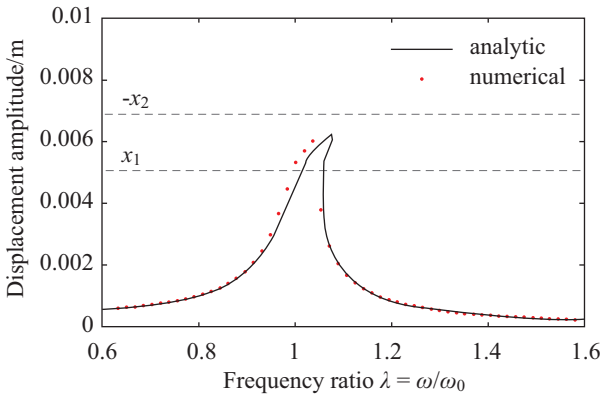


Fig. 9 Analytic FRF and numerical FRF of MSI system with initial condition (0, 0), $F/M = 0.12$.

$$\begin{cases} \Phi_1^2 + \Psi_1^2 + f_0^2 = 0, & (a < x_1) \\ \Phi_2^2 + \Psi_2^2 + f_0^2 = 0, & (x_1 < a < -x_2) \\ \Phi_3^2 + \Psi_3^2 + f_0^2 = 0, & (a > -x_2) \end{cases} \tag{23}$$

There are joints of the three parts at critical displacements x_1 and x_2. Fig. 10 compares the analytic FRF and numerical FRF of $A > -x_2$.

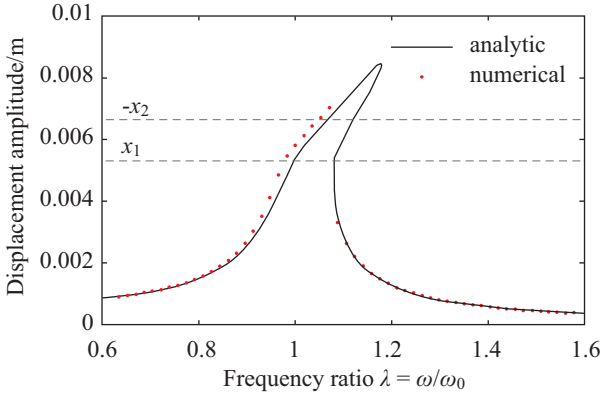


Fig. 10 Analytic FRF and numerical FRF of MSI system with initial condition (0, 0), $F/M = 0.18$.

From the comparison of the analytic FRF and numerical FRF, we can find good agreement for small amplitude vibration as shown in Fig. 8 and Fig. 9. The result is still acceptable for large amplitude vibration as shown in Fig. 10, considering that the averaging method only takes the first order approximation of the nonlinear system into account.

3.2 Phase Trajectories Diagram Evolvement

The phase trajectories diagram can be plotted by applying fourth order Runge-Kutta method to Eq. (6) and (7) and can be used to analyze jump phenomenon. Considering that the expressions of Φ and Ψ change when a crosses critical displacement, we substitute Eq. (13), (14), (16), (17), (19) and (20) into Eq. (6) and (7) to get piecewise differential equations of a and θ respectively. Phase trajectories from different initial point of (a, θ) can be plotted into one diagram by solving a and θ numerically (see Fig. 11).

Figure. 11A gives the analytic FRF curve. It can be observed from Fig. 11A that in the frequency near resonance, multiple solutions of FRF appears. Therefore, in the sweep sine test, the FRF curve is either A-B-C-E-F or F-E-D-B-A and a jump phenomenon arises. Fig. 11B~11F depict numerical phase trajectories diagram evolvement of MSI isolation system when excitation frequency increases. As shown in Fig. 11A, we define the excitation frequency as f and the frequency of points B and C as f_B and f_C. The phase trajectories diagram evolvement and jump phenomenon can be analyzed as follows.

If $f < f_B$, the FRF of MSI isolation system has an only solution in Fig. 11A, corresponding to a stable node P_1 in Fig. 11B. We can see from Fig. 11B that all trajectories spiral towards P_1.

If $f = f_B$, the FRF of MSI isolation system has two solutions (B and D in Fig. 11A). The phase trajectories under this excitation frequency are shown in Fig. 11C, from which we can see that there is a saddle-node P_{23} besides the node P_1. All trajectories are attracted to either P_1 or P_{23}. However, when a small disturbance applies on P_{23}, the system state will depart from P_{23} and be attracted to P_1.

If $f_B < f < f_C$, the FRF of MSI isolation system has three solutions (see Fig. 11A) because solution D has evolved into two solution branches BC and CD. At the same time, the saddle-node P_{23} has split into an unstable saddle P_2 and a stable node P_3 and the phase trajectories are attracted to either P_1 or P_3 (see Fig. 11D).

If $f = f_C$, the FRF of MSI isolation system has two solutions (points C and E, see Fig. 11A) as the solutions branches BC and CD have jointed at C. And in the phase trajectories diagram (see Fig. 11E), the saddle P_2 and node P_1 have combined into a saddle-node P_{12}. All trajectories are attracted to either P_{12} or P_3. When a small disturbance applies on P_{12}, the system state will depart from P_{12} and be attracted to P_3.

If $f > f_C$, the FRF of MSI isolation system has an only solution in Fig. 11A. All phase trajectories are attracted to the stable node P_3 as can be observed in Fig. 11F.

4. JUMP AVOIDANCE DESIGN OF MSI

There always exists jump phenomenon. For example, considering rotating equipment has to pass the resonance region during starting-up or running-down, the FRF curve is either A-B-C-E-F or F-E-D-B-A (see Fig.11A). Therefore, the vibration amplitude of rotating equipment will jump down at f_c when started-up and jump down at f_b when running down. These sudden changes of amplitude could bring up unexpected impact to the equipment. On the other hand, for some other equipment who takes advantage of vibration, such as shaker screen, a small disturbance of excitation frequency may lead to a jump down of amplitude, result in insufficient vibration for screening. Therefore, a properly designed vibration isolator should prevent jump from appearing and it is imperative to seek a design scheme under which jump phenomenon can be avoided best. Researchers such as

https://doi.org/10.1017/jmech.2016.52 Published online by Cambridge University Press

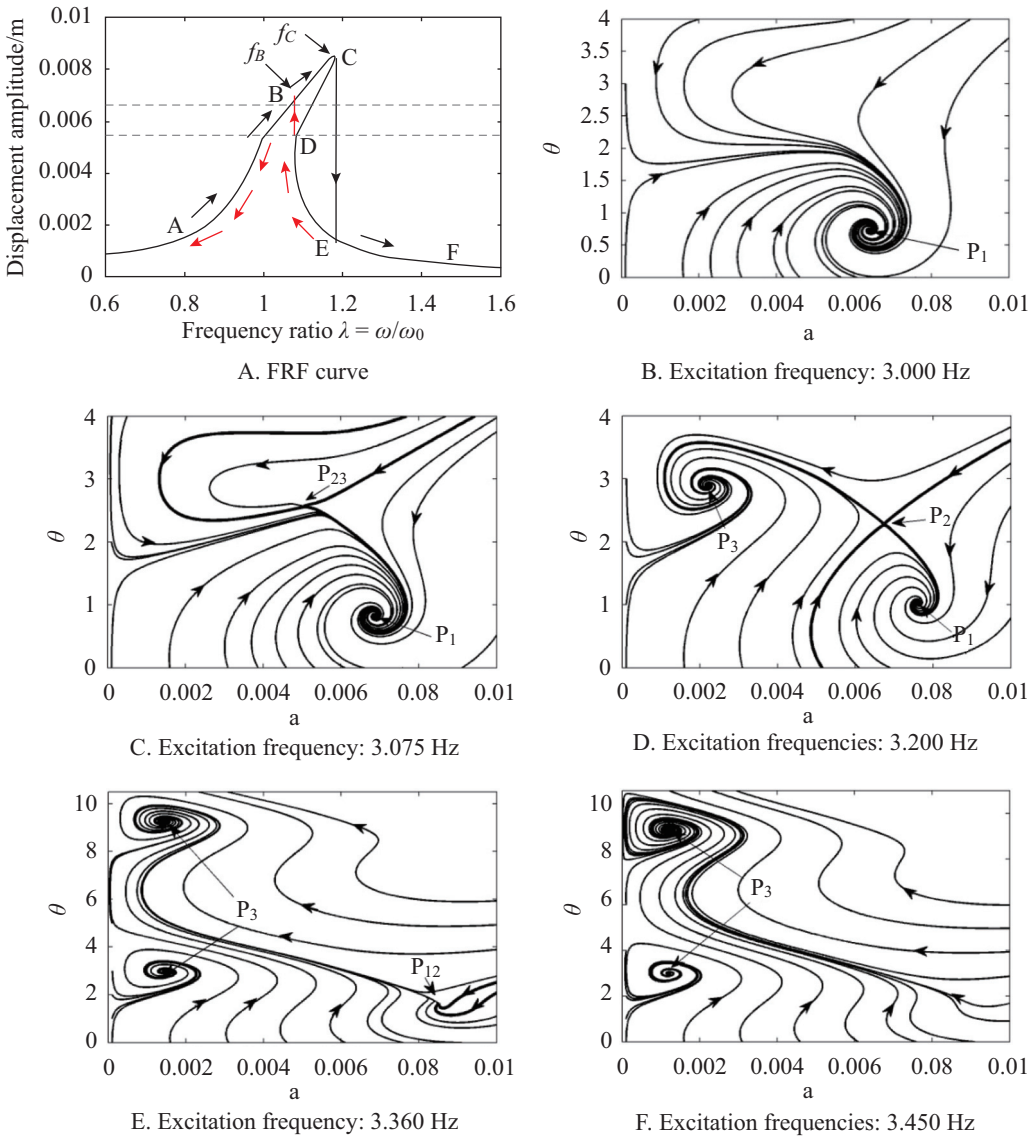


Fig. 11 FRFs curve and phase trajectories diagram evolvement of MSI system.

Worden [18] estimated jump-up and jump-down frequencies of a Duffing oscillator with linear viscous damping. Gao [16] and Jazar [19] gave the parameters boundary of jump avoidance for some piecewise linear systems. Although jump phenomenon has been researched in these literatures, this paper presents a novel MSI isolation system, which exhibits favorable high-static-low-dynamic stiffness properties. In this section, the value of excitation force, damping and the nonlinear stiffness are considered for jump avoidance design of MSI isolation system.

4.1 Force Stability Curve and Critical Value of Excitation Force

In Fig. 11A, there are at least two points in the FRF curve where $d\lambda/da = 0$. The jump phenomenon can be avoided if $d\lambda/da \neq 0$ in the whole frequency range. Hence the critical condition for jump avoidance is that the FRF curve has only one point to make $d\lambda/da = 0$.

Eq. (23) gives the whole FRF. We can derive $d\lambda/da$ by taken implicit differentiation of FRF

$$\frac{d\lambda}{da} = \begin{cases} DL_1, & (a < x_1) \\ DL_2, & (x_1 < a < -x_2) \\ DL_3, & (a > -x_2) \end{cases} \tag{24}$$

where DL_1, DL_2 and DL_3 are very complicated and given in appendix A. Notice that f_0 is eliminated during implicit differentiation, so there is no f_0 in the expressions of DL_1, DL_2 and DL_3. We make $d\lambda/da = 0$ and plot the equation piecewise into FRF curves diagram to get the force stability curve (see Fig. 12). The force stability curve divides the λ-a plane into a stable zone and an unstable zone. If the excitation force is large enough, the FRF curves are intersected into three parts by the force stability curve at the two vertical slopes, i.e. where $d\lambda/da = 0$. The unstable portion which will never be obtained experimentally is cut off from the FRF curves by the force stability curve [18].

https://doi.org/10.1017/jmech.2016.52 Published online by Cambridge University Press

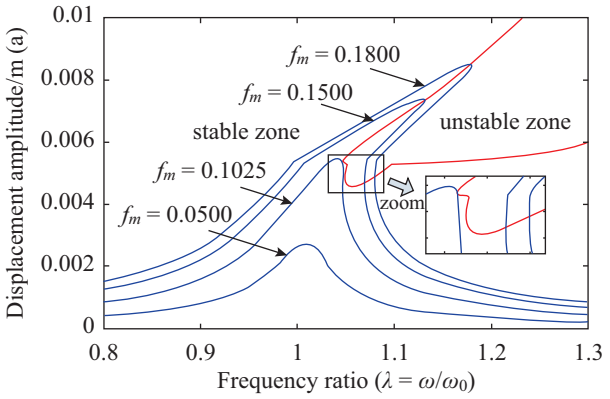


Fig. 12 Force stability curve and FRFs curves under different excitation force, f_m = 0.1025 is the critical value of excitation force (7.5 g zeolites is filled in MSI, c_0 = 1.0000).

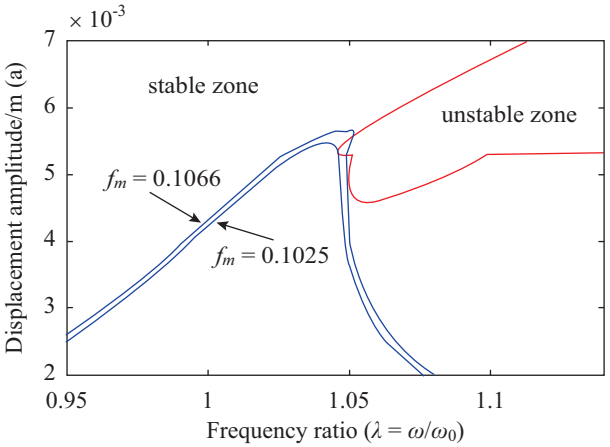


Fig. 13 The two points on force stability curve where $d\lambda/da = 0$; f_m = 0.1025 is the real critical value of excitation force (7.5 g zeolites is filled in MSI, c_0 = 1.0000).

There is a critical value of excitation force under which the FRF curve is tangent to the force stability curve. So there also will be a common tangent pass through the point of contact. For the FRF curve, $d\lambda/da$ is zero at the point of contact, and therefore the slope of the common tangent should be vertical too. Accordingly, at the point of contact, the slope of the force stability curve is also vertical. We can see from Fig. 13 that, on the force stability curve, there are two points who have vertical slope. Obviously, only the one within $x_1 < a < x_2$ is the real critical value of excitation force.

The point of contact is defined as (λ_{c1}, a_{c1}) and its coordinate can be obtained from stability curve. According to the value amplitude a_{c1}, choose to substitute λ_{c1} and a_{c1} into approprite Ψ_i and an Φ_i (i = 1, 2 or 3). And then substitute the Ψ_i and Φ_i into Eq. (10) hence we can get the critical value of excitation force.

From Fig. 12, we can conclude that for a MSI isolation system, the peak of displacement amplitude decrease when the excitation force decreases. Jump phenomenon can be avoided by decreasing excitation force to less than the critical value.

4.2 Damping Stability Curve and Critical Damping Coefficient

By solving the FRF Eq. (23), c_0 can be expressed as follows

$$c_0 = \begin{cases} \sqrt{-\dfrac{\Psi_1^2 + f_0^2}{a^2\lambda^2\omega_0^2}}, & (a < x_1) \\ \sqrt{-\dfrac{\Psi_2^2 + f_0^2}{a^2\lambda^2\omega_0^2}}, & (x_1 < a < -x_2) \\ \sqrt{-\dfrac{\Psi_3^2 + f_0^2}{a^2\lambda^2\omega_0^2}}, & (a > -x_2) \end{cases} \tag{25}$$

Substitute Eq. (25) into Eq. (24), so we can eliminate c_0 from Eq. (24). Make $d\lambda/da = 0$ and plot the equation, we can get the damping stability curve as shown in Fig. 14. The same with force stability curve, the damping stability curve also divides the λ-a plane into a stable and an unstable zone. The FRF curves are intersected into three parts by the damping stability curve at the two vertical slopes. A critical damping coefficient can be found when the damping stability curve is tangent to the FRF curve.

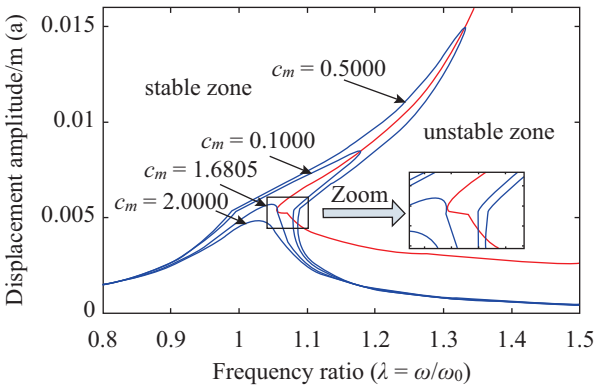


Fig. 14 Damping stability curve and FRFs curves under different excitation force, c_m = 1.6805 is the critical damping coefficient (7.5 g zeolites filled in MSI, f_m = 0.1800).

We can see form Fig. 14 that the peak of displacement amplitude decrease with the damping coefficient increase and jump phenomenon can be avoided by increasing damping coefficient till bigger than the critical value.

4.3 Influence of Nonlinear Stiffness (the Quantity of Zeolites) and Damping Coefficient on Jump Avoidance

As the nonlinear stiffness of MSI is determined by the quantity of zeolites [3-4], so the force stability curves of MSI filled with different quantity are investigated. Main parameters of MSI with different quantity of zeolites are given in table 1. At the same time, the stiffness curves of the vibration isolation system supported by these MSI are plotted in Fig. 15. It can be observed that

https://doi.org/10.1017/jmech.2016.52 Published online by Cambridge University Press

Table 1 Main parameters of MSI with different quantity of zeolites.

Quantity of zeolites/g	k_0 Nm^{-1}	α_1 Nm^{-1}	α_2 Nm^{-1}	α_3 Nm^{-1}	x_1 m	x_2 m
5	5.494×10^5	2.7141×10^5	-9.54347×10^{-6}	3.22077×10^8	4.4×10^{-3}	-6.5×10^{-3}
7.5	5.494×10^5	2.3411×10^5	-8.5079×10^{-6}	8.7465×10^8	5.3×10^{-3}	-6.7×10^{-3}
10	5.494×10^5	1.7909×10^5	-5.9740×10^{-6}	2.7149×10^8	6.9×10^{-3}	-8.8×10^{-3}

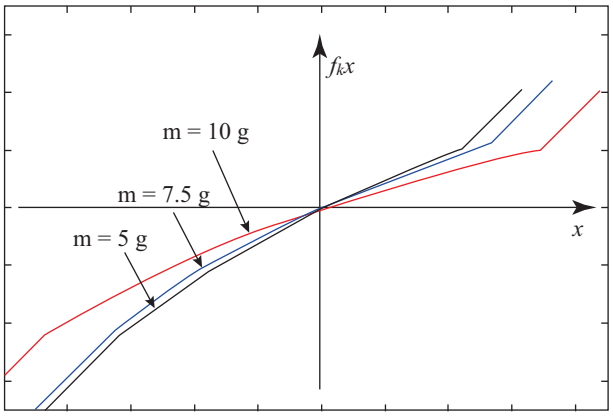


Fig. 15 Stiffness curve of the system supported by a MSI with different quantity of zeolites filled.

dynamic stiffness declines and the range of dynamic stiffness stage is broadened with the mass of zeolites increase.

Figure 16 plots the analytic force stability curves and critical FRF curves with different quantity of zeolites with c_m = 1.0000. The location of unstable zone, the point of contact and the peak of critical FRF curve all move up with quantity of zeolites increase. At the same time, the critical excitation force also increases. So jump phenomenon is more difficult to take place if MSI is filled with more zeolites when c_m = 1.0000.

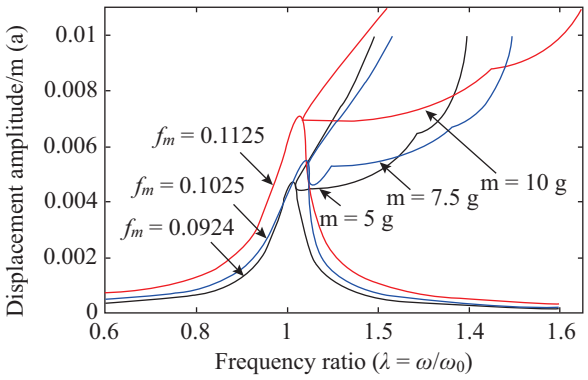


Fig. 16 Influence of quantity of zeolites on force stability curves and critical value of excitation force, (c_m = 1.0000).

However, situation gets different with smaller damping ratio (c_m = 0.5000). As shown in Fig. 17, the critical value of excitation force, f_m, is smaller when the quantity of zeolites increases from 5 g to 7.5 g. That is because with smaller damping ratio, critical FRF curve and force stability curve contact at the amplitude range $a < x_1$, giving a chance of smaller f_m with larger quantity of zeolites.

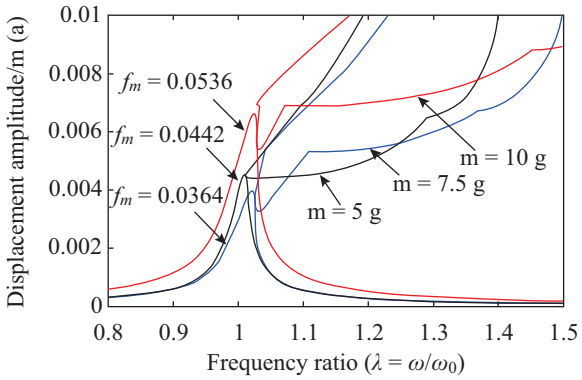


Fig. 17 Influence of quantity of zeolites on force stability curves and critical value of excitation force (c_m = 0.5000).

Figure 18 gives the analytic force stability curves and critical FRF curves with different damping coefficient. We can observe that unstable zone, especially the area in $a < x_1$ region, reduces with the damping coefficient increase. The force stability curves move to upper right direction and the critical excitation forces rise. Therefore, higher damping helps to avoid jump.

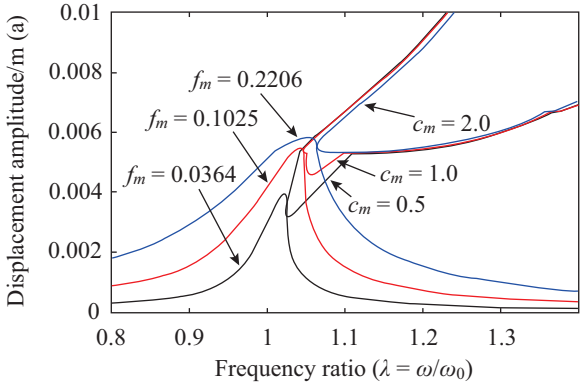


Fig. 18 Influence of damping on force stability curves and critical value of excitation force (7.5 g zeolites is filled in MSI).

https://doi.org/10.1017/jmech.2016.52 Published online by Cambridge University Press

Figure 19 plots the analytic damping stability curves and critical FRF curves with different quantity of zeolites. Fig. 19 shows that critical damping coefficient decrease with the quantity of zeolites increase, i.e. a MSI with more zeolites needs smaller damping coefficient to avoid jump under the same exaction. So larger quantity of zeolite helps to prevent jump phenomenon.

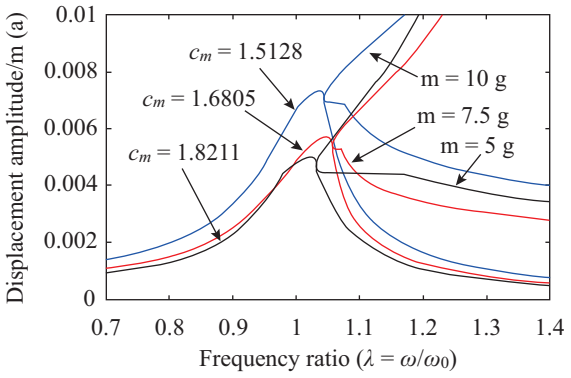


Fig. 19 Influence of quantity of zeolites on damping stability curves and critical damping coefficient (f_m = 0.1800).

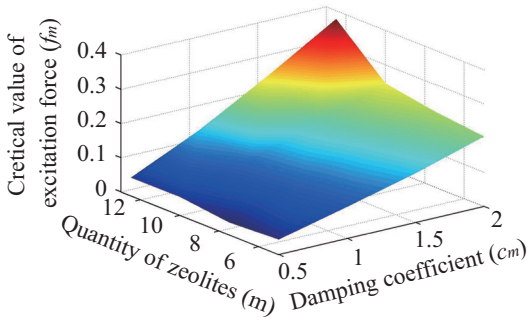


Fig. 20 Critical surface of jump avoidance, the surface gives the critical value of excitation force.

Figure 20 gives a critical surface of jump avoidance. Form Fig. 20 and the upper analysis, we can conclude that:

1. Jump phenomenon can be avoided if the excitation is smaller than critical value of excitation force;

2. Larger damping ratio help to avoid jump phenomenon;

3. the influence of the quantity of zeolites on jump phenomenon is complicated. When the damping ratio is big enough, more zeolites help to avoid jump, whereas it no longer valid for small damping ratio.

5. CONCLUSIONS

A MSI is a passive vibration isolation apparatus with high-static-low-dynamic stiffness properties. Different with traditional high-static-low-dynamic stiffness isolators using magnet [20] or multi-spring structures [21], the unique stiffness properties of MSI come from the special working mechanism and the characteristic of hydrophobic nanoporous material instead of complicated structures. So it has advantages of simple structure, small size and good flexibility to different environment conditions.

Averaging method is utilized in order to analyze the FRF and develop a dynamics design method for the MSI. By solving the FRF, we find that the FRF curves bend severely due to the strong nonlinearity, lending to a jump phenomenon, which could bring up unexpected damage to the system. Subsequently, the critical conditions to avoid jump phenomenon are investigated. It is found that the decrease of excitation force and the increase of damping ratio could help to avoid jump. However, the quantity of zeolites has more complicated influence on jump phenomenon. Nevertheless, the overall trend is that larger quantity of zeolites help to avoid jump phenomenon.

In summary, this paper provides a passive vibration isolation technology for heavy equipment with low frequency. The work helps designers to be familiar with dynamic properties of MSI and provides a guideline for engineers to select appropriate design parameters of MSI in practical applications.

ACKNOWLEDGEMENTS

This work was supported by National Natural Science Foundation of China under Grant No. 11272145 and 11472127, Funding of Jiangsu Innovation program for Graduate Students under Grant No. CXLX13_134, the Fundamental Research Funds for the Central Universities and A Project Funded by the Priority Academic Program Development of Jiangsu Higher Education Institutions (PAPD).

https://doi.org/10.1017/jmech.2016.52 Published online by Cambridge University Press

APPENDIX A

$$\text{(A1)}: \quad DL_1 = \frac{16\sigma^2 - 48\sigma r_3 a^2 + 27 r_3^2 a^4 + 16 {c_0}^2 \lambda^2 {\omega_0}^2}{-16 {c_0}^2 a \lambda {\omega_0}^2}$$

$$\begin{aligned}
DL_2 = {} & \frac{1}{-144 {c_0}^2 a^2 \lambda {\omega_0}^2 \pi^2} (-432\sigma a^3 \pi^2 r_3 - 486 {r_3}^2 a^5 \gamma_1 \pi + 144 a \omega_0^4 \gamma_1^2 + 243 r_3^2 a^5 \gamma_1^2 \\
& + 512 a^3 r_2^2 R_1^2 - 648 \omega_0^2 x_1 R_1 r_3 a^2 \gamma_1 - 384 \omega_0^2 x_1 R_1^2 a r_2 - 216 \omega_0^2 {x_1}^2 R_1^2 a r_3 - 576 a^2 \omega_0^2 \gamma_1 r_2 R_1 \\
& - 648 fc_1 R_1 r_3 a^2 \gamma_1 - 432 fc_1 R_1^2 r_3 a x_1 - 96 r_2 {x_1}^2 R_1 \omega_0^2 \gamma_1 + 216 r_2 R_1 r_3 a^2 \gamma_1 + 336 r_2 {x_1}^3 R_1^2 r_3 a \\
& + 720 r_3 a^4 \gamma_1 r_2 R_1 + 405 R_3^2 a^4 \gamma_1 x_1 R_1 + 576 a^3 r_2 R_1^2 r_3 x_1 - 72 r_3 {x_1}^2 R_1 \omega_0^2 \gamma_1 + 162 r_3^2 {x_1}^3 R_1 a^2 \gamma_1
\end{aligned}$$

$$\begin{aligned}
\text{(A2)}: \quad & -768 fc_1 R_1^2 r_2 a + 288 fc_1 r_1 \omega_0^2 \gamma_1 - 432 a^3 \omega_0^2 {\gamma_1}^2 r_3 + 144 \omega_0^2 x_1 R_1 \gamma_1 + 256 r_2^2 {x_1}^2 R_1^2 a + 144 \sigma^2 a \pi^2 \\
& + 243 r_3^2 a^5 \pi^2 - 288 fc_1 R_1 \sigma \pi - 144 \omega_0^2 x_1 R_1 \sigma \pi + 324 \omega_0^2 x_1 R_1 r_3 a^2 \pi - 288 a \omega_0^2 \gamma_1 \sigma \pi \\
& + 432 a^3 \omega_0^2 {\gamma_1}^2 r_3 \pi + 648 fc_1 R_1 r_3 a^2 \pi + 96 r_2 {x_1}^2 R_1 \sigma \pi - 216 r_2 {x_1}^2 R_1 r_3 a^2 \pi + 432 r_3 a^3 \gamma_1 \sigma \pi \\
& + 576 a^2 r_2 R_1 \sigma \pi - 720 a^4 r_2 R_1 r_3 \pi + 72 r_3 {x_1}^3 R_1 \sigma \pi - 162 r_3^2 {x_1}^3 R_1 a^2 \pi + 324 x_1 R_1 r_3 a^2 \sigma \pi \\
& - 405 r_3^2 a^4 x_1 R_1 \pi + 162 r_3^2 a^3 {x_1}^2 {R_1}^2 + 108 r_3^2 {x_1}^4 {R_1}^2 a + 144 c_0^2 a \lambda^2 \omega_0^2 \pi^2)
\end{aligned}$$

$$\begin{aligned}
DL_3 = {} & \frac{1}{-144 {c_0}^2 a^2 \lambda {\omega_0}^2 \pi^2} (144 \omega_0^4 x_2 R_2 \gamma_2 - 144 \omega_0^4 x_2 R_2 \gamma_1 + 768 fc_1 R_2 a r_2 R_1 + 288 fc_2 R_2 \omega_0^2 \gamma_2 \\
& - 144 r_2 x_2^2 R_2 r_3 a x_1 R_1 - 768 fc_2 {R_2}^2 a r_2 - 288 fc_2 R_2 \omega_0^2 \gamma_1 - 432 fc_2 R_2^2 r_3 a x_2 + 384 \omega_0^2 x_2 R_2 a r_2 R_1 \\
\text{(A3)}: \quad & -144 r_2 x_1^2 r_3 R_1 a x_2 R_2 + 432 \omega_0^2 x_2 R_2 a r_3 x_1 R_1 + 432 fc_2 R_2 a r_3 x_1 R_1 - 216 \omega_0^2 x_2^2 R_2^2 a r_3 - 648 fc_2 R_2 a^2 r_3 \gamma_2 \\
& + 648 fc_2 R_2 a^2 r_3 \gamma_1 - 1024 a^3 r_2^2 R_2 R_1 + 144 a \omega_0^4 \gamma_2^2 + 512 a^3 r_2^2 R_2^2 + 243 r_3^2 a^5 \gamma_2^2 - 144 \omega_0^4 x_1 R_1 \gamma_2 \\
& - 384 \omega_0^2 x_2 R_2^2 a r_2 + 144 a \omega_0^4 \pi + 576 a^2 r_2^2 R_1 \omega_0^2 \gamma_2 - 720 a^4 r_2 R_1 r_3 \gamma_2 + 256 r_2^2 x_2^2 R_2^2 a + 384 \omega_0^2 x_1 R_2 R_1 a r_2 \\
& + 648 \omega_0^2 x_1 R_1 r_3 a^2 \gamma_2 - 720 a^4 r_3 R_2 r_2 \gamma_1 + \ldots\ldots)
\end{aligned}$$

REFERENCES

1. Gao, X., Chen, Q. and Teng, H.D., "Molding and dynamics properties of a novel solid and liquid mixture vibration isolation," *Journal of Sound and Vibration*, **331**, pp. 3695-3709 (2012).
2. Teng, H.D. and Chen, Q., "Study on vibration isolation properties of solid and liquid mixture," *Journal of Sound and Vibration*, **329**, pp. 137-149 (2009).
3. Yu, M.C., Chen, Q., Gao, X. and Zhang, S. Z., "Investigation of molecular spring on vibration isolation mechanism and mechanical properties," *Chinese Journal of Theoretical and Applied Mechanics*, **46**, pp. 553-560 (2014).
4. Yu, M.C., Chen, Q. and Gao, X., "Theoretical and Experimental Investigation of Molecular Spring Isolator," *Microsystem Technologies*, DOI: 10.1007/s00542-014-2401-7 (2015).
5. Fadeev, A., and Eroshenko, V., "Study of penetration of water into hydrophobized porous silicas," *Journal of Colloid and Interface Science*, **187**, pp. 275-282 (1997).
6. Suciu, C. and Iwatsubo, T., "Investigation of a colloidal damper," *Journal of Colloidal and Interface Science*, **259**, pp. 62-80 (2001).
7. Suciu, C., Iwatsubo, T., Yaguchi, k. and Ikenaga, M., "Novel and global approach of the complex and interconnected phenomena related to the contact line movement past a solidsurface from hydrophobized silica gel," *Journal of Colloid and Interface Science*, **283**, pp. 196-214 (2005).
8. Kong, X., Surani, F. B. and Qiao, Y., "Energy absorption of nano-porous silica particles in aqueous solutions of sodium chloride," *Physic Scripta*, **7**4, pp. 531-534 (2006).
9. Han, A., Kong, X., and Qiao, Y., "Pressure induced liquid infiltration in nanopores," *Journal of Applied Physics*, **100**, pp. 1-3 (2006).
10. Eroshenko, V., Regis, R., Soulard, M. and Patarin, J., "Energetic: a new field of application of hydrophobic zeolites," *Journal of The American Chemical Society*, **123**, pp. 8129-8130 (2001).

https://doi.org/10.1017/jmech.2016.52 Published online by Cambridge University Press

11. Soulard, M., Patarin, J., Eroshenko, V. and Regis, R., "Molecular spring or bumper: a new application for hydrophobic zeolites materials," *Studies in Surface Science and Catalysis*, **154**, pp. 1830-1837 (2004).
12. Trzpit, M., Rigolet, S. and Paillaud, J., "Pure silica chabazite molecular spring: a structural study on water intrusion-extrusion processes," *Journal of Physical Chemistry*, **112**, pp. 7257-7266 (2008).
13. Tzanis, L., Trzpit, M., Soulard, M. and Patarin, J., "High pressure water intrusion investigation of pure silica 1D channel AFI, MTW and TON-type zeolites," *Microporous and Mesoporous Materials*, **146**, pp. 119-126 (2011).
14. Tzanis, L., Trzpit, M., Soulard, M. and Patarin, J., "Energetic Performances of Channel and Cage-Type Zeosils," *Journal of Physical Chemistry*, **116**, pp. 20389-20395 (2012).
15. Desbiens, N., Boutin, A. and Demachy, I., "Water condensation in hydrophobic Silicalite-1 zeolite: a molecular simulation study," *Journal of Physical Chemistry*, **109**, pp. 24071-24076 (2005).
16. Gao, X. and Chen, Q., "Nonlinear frequency response analysis and dynamics design of a solid and liquid mixture nonlinear vibration isolator," *Journal of Vibration and Control*, **20**, pp. 2389-2400 (2014).
17. McCusker, L.B., Liebau, F. and Engelhardt, G., "Nomenclature of structural and compositional characteristics of ordered microporous and mesoporous materials with inorganic hosts (IUPAC recommendations 2001)," *Microporous and Mesoporous Materials*, **58**, pp. 3-13 (2003).
18. Worden, K., "On jump frequencies in the response of the duffing oscillator," Journal *of Sound and vibration*. **198**, pp. 522-525 (1996).
19. Jazar, G.N., Houim, R., Narimani, A. and Golnaraghi, M. F., "Frequency response and jump avoidance in a nonlinear passive engine mount," *Journal of Vibration and Control*, **12**, pp. 1205-1237 (2006).
20. Zhou, N. and Liu, K., "A tunable high- static–low-dynamic stiffness vibration isolator," *Journal of Sound and Vibration*, **329**, pp. 1254-1273 (2010).
21. Carrella, A., Brennan, M., Waters, T. P. and Lopes, V., "Force and displacement transmissibility of a nonlinear isolator with high-static-low-dynamic-stiffness," *International Journal of Mechanical Sciences*, **55**, pp. 22-29 (2012).

(Manuscript received July 15, 2015,
accepted for publication March 16, 2016.)

https://doi.org/10.1017/jmech.2016.52 Published online by Cambridge University Press